
HIGH-RESOLUTION SYNTHESIS OF HIGH-DENSITY BREAST MAMMOGRAMS: APPLICATION TO IMPROVED FAIRNESS IN DEEP LEARNING BASED MASS DETECTION

Lidia Garrucho*

Facultat de Matemàtiques i Informàtica
Universitat de Barcelona
Barcelona, Spain

Kaisar Kushibar

Facultat de Matemàtiques i Informàtica
Universitat de Barcelona
Barcelona, Spain

Richard Osuala

Facultat de Matemàtiques i Informàtica
Universitat de Barcelona
Barcelona, Spain

Oliver Diaz

Facultat de Matemàtiques i Informàtica
Universitat de Barcelona
Barcelona, Spain

Alessandro Catanese

Unitat de Diagnòstic per la Imatge de la Mama
Hospital Germans Trias i Pujol
Badalona, Spain

Javier del Riego

Àrea de Radiologia Mamària y Ginecològica
Parc Taulí Hospital Universitari
Sabadell, Spain

Maciej Bobowicz

2nd Department of Radiology
Medical University of Gdansk
Gdansk, Poland

Fredrik Strand

Breast Radiology, Karolinska University Hospital
Department of Oncology-Pathology, Karolinska Institutet
Stockholm, Sweden

Laura Igual

Facultat de Matemàtiques i Informàtica
Universitat de Barcelona
Barcelona, Spain

Karim Lekadir

Facultat de Matemàtiques i Informàtica
Universitat de Barcelona
Barcelona, Spain

September 21, 2022

ABSTRACT

Computer-aided detection systems based on deep learning have shown good performance in breast cancer detection. However, high-density breasts show poorer detection performance since dense tissues can mask or even simulate masses. Therefore, the sensitivity of mammography for breast cancer detection can be reduced by more than 20% in dense breasts. Additionally, extremely dense cases reported an increased risk of cancer compared to low-density breasts. This study aims to improve the mass detection performance in high-density breasts using synthetic high-density full-field digital mammograms (FFDM) as data augmentation during breast mass detection model training. To this end, a total of five cycle-consistent GAN (CycleGAN) models using three FFDM datasets were trained for low-to-high-density image translation in high-resolution mammograms. The training images were split by breast density BI-RADS categories, being *BI-RADS A* almost entirely fatty and *BI-RADS D* extremely dense breasts. Our results showed that the proposed data augmentation technique improved the sensitivity and precision of mass detection in high-density breasts by 2% and

*Corresponding author: lgarrucho@ub.edu

6% in two different test sets and was useful as a domain adaptation technique. In addition, the clinical realism of the synthetic images was evaluated in a reader study involving two expert radiologists and one surgical oncologist.

Keywords Data synthesis · Full-field Digital Mammograms · Generative Adversarial Networks · Data augmentation · Mass detection · Reader study · Breast cancer

1 Introduction

Breast density is divided into four categories in the American College of Radiology Breast Imaging and Data System (ACR BI-RADS) 5th edition [1]. The categories range from A to D and correspond to fatty, scattered, heterogeneous, and extremely dense breasts. The qualitative classification of breast density in mammography is an accepted method in breast radiology with good inter-observer and intra-observer agreement [2], despite the fact that commercial software can produce a more accurate quantitative measure by calculating the ratio of fibroglandular tissue to the total breast area.

In mammography databases, the distribution of breast densities among women aged 40 years or older is approximately 43% for dense breasts: 36% for BI-RADS C and 7% for BI-RADS D [3]. [4] found that women with a family history of breast cancer were more likely to have dense breasts than women with no cancer in the family history. In addition, high breast density is associated with an increased risk of interval cancers [5], being those 13–31 times more likely in BI-RADS D breasts than in BI-RADS A [6, 7, 8]. Consequently, it is recommended to decrease the interval between screening mammograms and consider supplemental screening for women with dense breasts [9, 8].

Dense breast tissue is one of the strongest and most common independent risk factors for breast cancer [10, 6, 5]. On mammograms, masses and other suspicious findings can be obscured in normal dense tissue and become imperceptible on mammograms. Therefore, the sensitivity of mammography decreases with increasing breast density and has a range value of 81–93% for fatty breasts, 84–90% for breasts with scattered fibroglandular density, 69–81% for heterogeneously dense breasts, and 57–71% for extremely dense breasts in women 40–74 years of age [5]. Although mammography is the gold standard non-invasive method for breast cancer detection in population-based screening, women with dense breasts have shown both a reduced cancer detection and higher mortality rates [11, 12, 13].

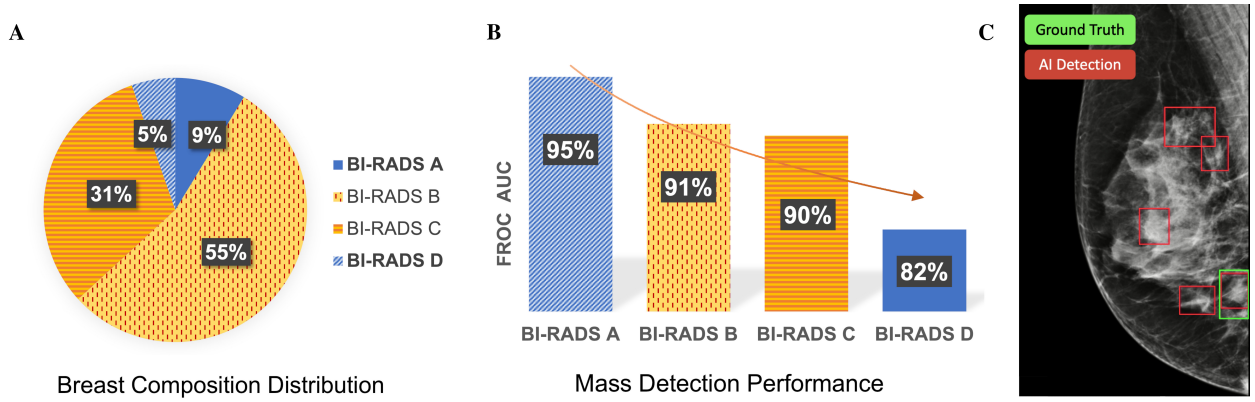


Figure 1: Differences in sensitivity of a deep learning-based mass detection model by breast density composition in full-field digital mammography. (A) Breast composition distribution of the training set. (B) Mass detection sensitivity by breast density. (C) Output of an automated detection model in a high-density (BI-RADS D) image. The red bounding boxes are the AI model outputs and the green box corresponds to the true mass, summing a total of four false positives.

The goal of this study is two-fold. First, mitigation of the differences in computer-aided detection (CADe) systems sensitivity by breast density [14]. Figure 1 shows the differences in sensitivity of our deep learning-based mass detection model density composition. The breast composition distribution of the dataset used to train the model has a big unbalance in categories A (9%) and B (5%) (Figure 1:A). Nonetheless, the sensitivity between fatty (95% for BI-RADS A) and extremely dense breasts (82% for BI-RADS D) (Figure 1:B). The decrease in performance is partly caused by the high rate of false positives in extremely dense breasts, as can be seen in Figure 1:C. Second, performance improvement of state-of-the-art deep learning-based breast mass detection models by the means of synthetic data augmentation. Data augmentation is used to increase the variability of the training samples, improve the model generalization and avoid

overfitting. Among all deep learning-based augmentation techniques, Generative Adversarial Networks (GANs) [15] are frequently used to generate new synthetic samples in an unsupervised manner. GANs have been previously used to synthesize full-field digital mammograms (FFDMs) or lesion patches, normally at low resolutions [16, 17, 18].

Becker et al [19] trained a cycle-consistent GAN (CycleGAN) on downsampled mammograms (256×256 and 512×408 pixels) to artificially inject or remove suspicious features. In their reader study, three radiologists could discriminate between original and synthetic images with an area under the curve (AUC) of 0.94, mainly due to the presence of artifacts. Zakka et al [20] trained a style-based GAN to generate 512×512 mammograms enabling user-controlled global and local attribute-editing. Then, a double-blind study involving four expert radiologists assessed the quality of the resulting images achieving an average AUC of 0.54.

Other studies used the synthetic mammograms as data augmentation to improve the performance in different downstream tasks. Synthetic data augmentation using GANs was evaluated in breast cancer classification by Shrinivas et al [21]. The proposed model, a Deep Convolutional GAN (DCGAN), synthesized FFDM with 256×256 image resolution. The synthetic images were validated using a Visual Turing test with the help of medical experts and were easily spotted by the radiologist because they lacked the sharpness and fine-grained details of original mammograms. In a similar study, Jendele et al [22] balanced the ratio of benign and malignant lesions in the training set using a CycleGAN trained to translate healthy mammograms to mammograms containing malignant findings. The synthetic mammograms were 256×256 pixels, as higher image resolutions introduced many artifacts. The benefits of using the synthesized mammograms for data augmentation were inconclusive considering that the performance of their detection model did not improve. Muramatsu et al [23] trained a CycleGAN using masses from unrelated domains – lung CT and mammography – to synthesize 256×256 pixels masses and improve the mass classification in mammography. However, no statistical difference was found between the model trained with synthetic masses and the classifier trained with original mass patches.

In this study, the original resolution of FFDMs, around 5 Megapixels (MP), with image sizes of 3328×4084 or 2560×3328 pixels depending on the manufacturer. Two main challenges have prevented the use of GANs for high-resolution FFDM synthesis. The first one is the high demand for graphics processing unit (GPU) memory, which typically scales with the input and output resolutions. As an example, CycleGAN needs more than 24GB of GPU memory when the input image is larger than 1MP. The second challenge is data scarcity. The training set has to be representative enough to generate realistic samples and overcome the training instabilities and image artifacts of GANs. High intrinsic heterogeneity exists across mammograms due to the huge variability of breast sizes, shapes, and compositions. Moreover, FFDMs contain very fine structural details at high resolution such as the different parenchymal patterns, nipples, and pectoral muscles, the presence of lymph nodules, microcalcifications, or calcifications, among many other associated features.

Korkinof et al [24] was the first study that managed to synthesize high-resolution FFDM images using a Progressively Growing GAN (PGGAN) [25]. Their PGGAN was trained using more than 400,000 FFDMs and was demonstrated to generate mammograms up to a 1280×1024 pixel resolution. All mammograms available were used for training, independently of the clinical findings, and only images with post-operative artifacts and large foreign bodies such as implants were excluded from the training set. In a separate retrospective study, Kornikof et al [26] evaluated the perceived realism of the synthetic FFDM images in a reader study involving 55 radiologists and 62 non-radiologists. Overall, in the setup of this study, the synthetic images were shown to be indistinguishable from original mammograms. However, it was unclear and was not further investigated whether the synthetic FFDMs have relevant applications for clinical purposes.

This work presents for the first time the use of GAN models to generate high-resolution FFDMs with increased breast density using images from different manufacturers. Moreover, we evaluated the potential of using the synthesized images as data augmentation to improve the mass detection performance. Only a single prior study had performed similar data augmentation by breast density categories for improved mass detection [27]. However, the authors employed mathematical breast phantoms generated using the pipeline in the VICTRE study [28] instead of GANs. The breast phantoms were generated across the four BI-RADS breast density categories for each view, cranio-caudal (CC) and mediolateral oblique (MLO), and were modeled after a single vendor, the Siemens Mammomat Inspiration. The limitations of their study is the lack of diversity within each density type, including the size and shape of the breast. Moreover, the statistical analysis did not show a significant difference between the free-response receiver operating characteristic (FROC) curves for mass detection.

To summarize, the contributions of our study are as follows:

- Synthesize high-resolution high-density FFDMs using GAN-based models from 3 different datasets and mammography systems (manufacturers).

- Tackle the class imbalance by breast density composition by augmenting the training set using high-density synthetic mammograms.
- Improve the performance of mass detection in extremely dense breasts, categorized as BI-RADS D.
- Investigate the potential of high-density data augmentation for domain adaptation.
- Evaluate the anatomical realism of the synthetic mammograms in a reader study involving 2 expert radiologists and 1 surgical oncologist.

2 Materials and Methods

2.1 Datasets and Breast Density

Four different datasets were used in this study, three of them for training the proposed models and one for mass detection evaluation. General details of these datasets are presented in table 1.

Table 1: The digital mammography datasets used for training the models. For each dataset, the total number of normal mammograms (MMG) and the available breast density information are mapped to the corresponding BI-RADS category. In OPTIMAM Hologic, the Volumetric Breast Density (VBD) percentage was obtained using Volpara software. In CSAW, the breast percentage was obtained running LIBRA software. In BCDR, the BI-RADS categories are available in the dataset information.

	OPTIMAM			CSAW		BCDR	
	Volpara VBD (%)	Normal MMG	MMG with masses	LIBRA (%)	Normal MMG	ACR	Normal MMG
BI-RADS A	≤ 3.5	972	344	≤ 2.8	435	1	40
BI-RADS B	(3.5, 7.5)	3670	1740	(2.8, 25)	52064	2	40
BI-RADS C	(7.5, 15.5)	1987	808	(25, 75)	38545	3	62
BI-RADS D	≥ 15.5	708	161	≥ 75	394	4	58

The OPTIMAM Mammography Image Database (OMI-DB) [29] comprises FFDM from the Breast Screening Programme of the United Kingdom (UK). In this study, we used the subset of mammograms captured with the Hologic Selenia Dimensions scanners (Hologic, Inc., Massachusetts, United States) as described in table 1. The proportion of fibroglandular (dense) tissue in the breast was obtained from the commercial Volpara software (version 1.5.4.0; Volpara Health, Wellington, New Zealand). The Volumetric Breast Density (VBD) percentage of each mammogram was mapped to the corresponding BI-RADS breast density category. Only normal mammograms – without pathologies – were selected to train the synthetic data generation models. Moreover, the mammograms containing masses were used to train the mass detection AI model.

The non-hidden case-control dataset of the CSAW dataset [30] was also used in this study. The dataset comprises screening FFDMs from Karolinska University Hospital (Solna, Sweden) acquired with Hologic Inc. devices. A total of 91,484 normal FFDM contained breast density information estimated using the LIBRA automated tool (University of Pennsylvania, United States) [31]. The mapping between LIBRA breast density percentage and BI-RADS A and D categories was done by selecting the tails of the percent density distribution of the healthy exams.

The Breast Cancer Digital Repository (BCDR) dataset [32] is a public dataset from 2012 comprising images supplied by the Centro Hospitalar São João, at University of Porto (Portugal) and obtained using a MammoNovation Siemens FFDM scanner. For our purposes, we selected a total of 200 FFDMs without pathologies. The breast density categories were provided in the annotations of the dataset following the American College of Radiology (ACR) statement on reporting breast density [1].

The INbreast dataset [33] was acquired from a single Portuguese center using a FFDM system, the Siemens MammoNovation. This public dataset was used for evaluating the mass detection model in an external domain not seen during the model training. INbreast contains 108 FFDMs with 116 annotated masses from different breast densities. The percentage of images in each BI-RADS category is 36%, 35%, 22% and 7% for BI-RADS A, B, C and D.

Images have a matrix of 3328×4084 or 2560×3328 pixels, depending on the compression plate used for image acquisition. In a previous work, we confirmed that a resolution of 1332×800 pixels was enough to detect small masses and reach state-of-the-art performance in different AI detection methods [34]. All the FFDM images were cropped to the breast region and resized to 1332×800 pixels keeping the aspect ratio. Our target resolution for data synthesis was the same as the one used by our deep learning mass detection model.

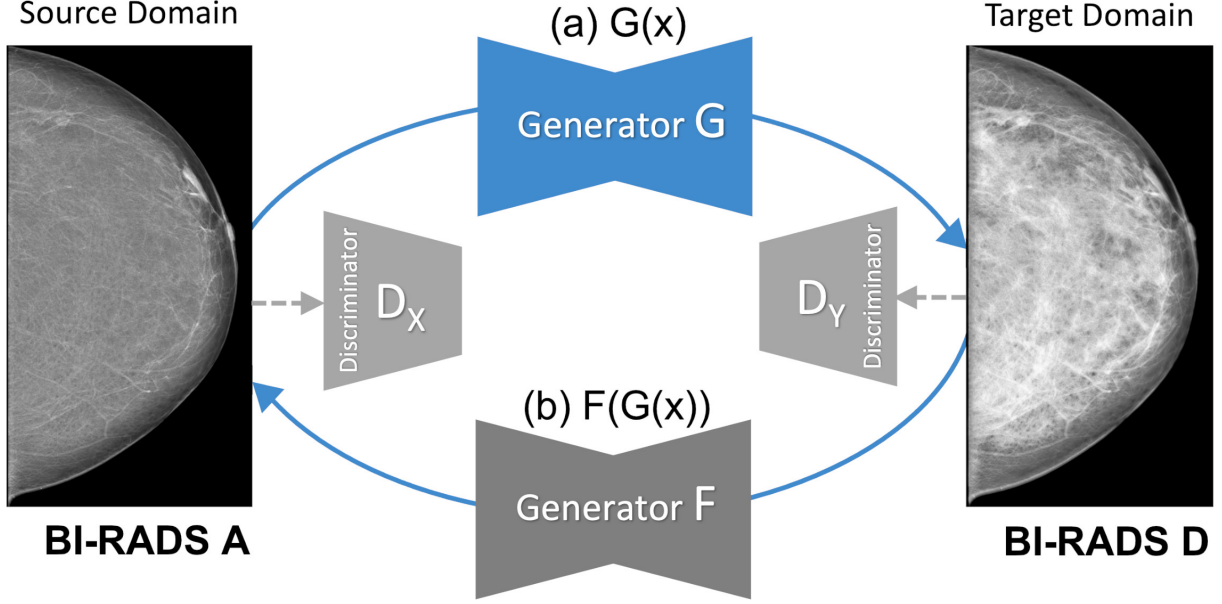


Figure 2: Overview of the mapping functions of the CycleGAN framework. (a) shows the mapping of a low-density mammogram (source domain) via generator G to a high-density mammogram (target domain). (b) depicts the mapping of a synthetic high-density mammogram back to the low-density source domain via generator F .

2.2 Synthesis of High-Density Full-Field Digital Mammograms

Our goal was to synthesise high-density FFDM from original low density mammograms and then use the synthetic data to improve the performance of our mass detection models.

To this end, the training images were split by breast density BI-RADS categories, being *BI-RADS A* the source domain and *BI-RADS D* the target domain. Before training, all mammogram images were resized to the target resolution (1332×800 pixels), the input size of the mass detection model.

The CycleGAN [35] was the method selected to perform the low-to-high-density mammogram translation. The choice of cycleGAN was motivated by its widespread use and successes reported in the cancer imaging domain [17]. A key methodological feature of CycleGAN is that its training data can be unpaired without the need for corresponding image pairs in source and target domains. Unpaired training data ensured the applicability of CycleGAN to our datasets, in which image pairs are not available, as the same breast of the same patient cannot be from both the high and the low breast density domains.

As shown in Figure 2, the CycleGAN contains two mapping functions: 1) an image x in the source domain is mapped to a synthetic image $G(x) = \hat{y}$ in the target domain via a generator G ; and 2) an image y is mapped from target to source $F(y) = \hat{x}$ via a generator F . This enables translating images from source to target and back to the source domain $F(G(x)) = \hat{x}$. Both generators F and G are paired with corresponding discriminators, which try to classify whether a generated image is real or synthetic in a two-player *minmax* game with their respective generator [15]. Based on the predictions of the discriminator, binary cross entropy is used to compute the adversarial loss as shown below, which is back-propagated to the respective generator network.

$$\mathcal{L}_{\text{GAN}}(G, D_Y, X, Y) = \mathbb{E}_{y \sim p_{\text{data}}(y)} [\log D_Y(y)] + \mathbb{E}_{x \sim p_{\text{data}}(x)} [\log(1 - D_Y(G(x)))]$$

CycleGAN further contains two cycle-consistency losses defined as $L1$ reconstruction loss between (i) the source image x and the reconstructed source image $F(G(x)) = \hat{x}$ and between (ii) the target image y and the reconstructed target image $G(F(y)) = \hat{y}$.

$$\mathcal{L}_{\text{cyc}}(G, F) = \mathbb{E}_{x \sim p_{\text{data}}(x)} [\|F(G(x)) - x\|_1] + \mathbb{E}_{y \sim p_{\text{data}}(y)} [\|G(F(y)) - y\|_1]$$

As defined by [35], the full loss function of our cycleGAN reads as follows with the λ parameter ($\lambda = 10$) weighting the relative importance between cycle-consistency and adversarial losses.

$$\mathcal{L}(G, F, D_X, D_Y) = \mathcal{L}_{\text{GAN}}(G, D_Y, X, Y) + \mathcal{L}_{\text{GAN}}(F, D_X, Y, X) + \lambda \mathcal{L}_{\text{cyc}}(G, F)$$

Only healthy mammograms (Normal) were used to train the different cycleGAN models. The main reason was to avoid feature hallucinations that have been shown to occur in cancer imaging when training on images where tumors were present [36, 17].

A total of five CycleGAN models from the three different datasets in Table 1 were trained (see Figure3). For the OPTIMAM and the CSAW dataset, a different model was trained for each view (CC and MLO). That was because the anatomic features of CC and MLO are different and more specialized CycleGAN models – focusing only on one view – should learn better translations. However, the small sample size in BCDR dataset made it unfeasible to split the models by view and, for this dataset, a single model was trained combining both CC and MLO views (Figure3:A).

The models were trained using a single GPU (24GB NVIDIA GeForce RTX 3090) for a maximum of 200 epochs, using a batch size of 1 and adjusting the learning rate following the recommendations implemented in the CycleGAN Pytorch framework.

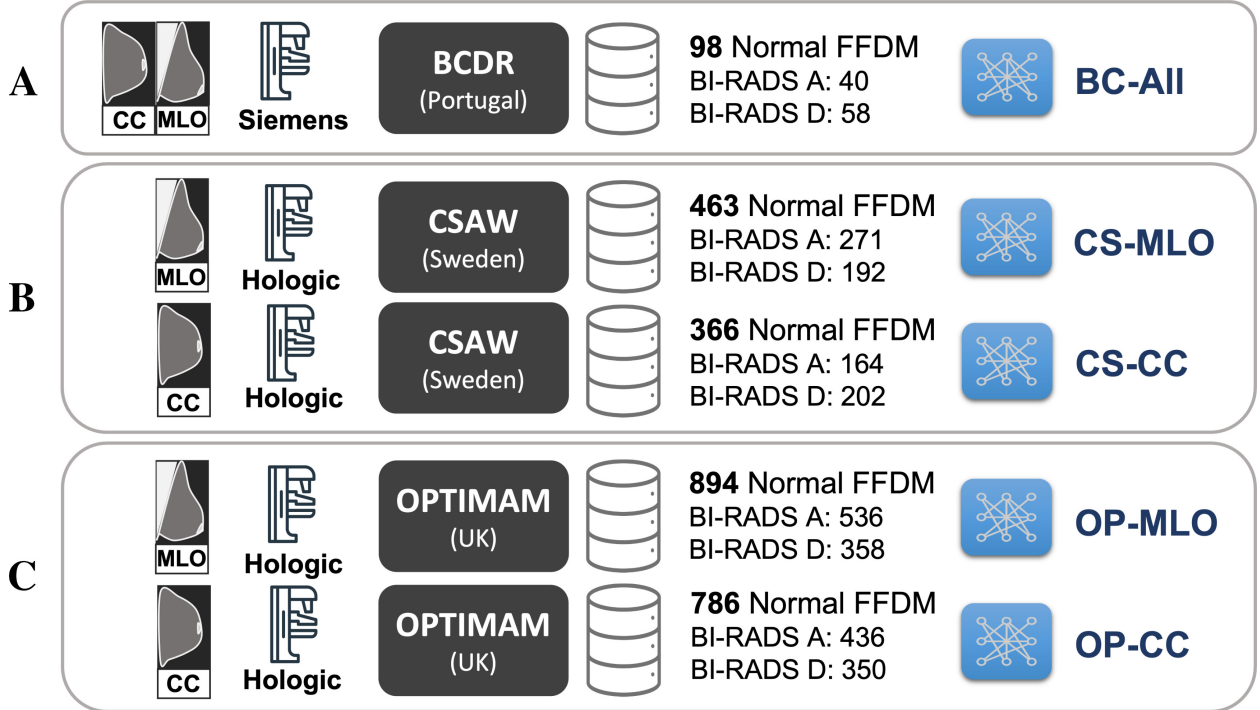


Figure 3: Training setup for the different CycleGAN models. (A) *BC-All* model for both CC and MLO views trained with 98 normal FFDMs from BCDR dataset. (B) two models for CC (*CS-CC*) and MLO (*CS-MLO*) views trained with 463 and 366 normal FFDMs from CSAW dataset. (C) two models for CC (*OP-CC*) and MLO (*OP-MLO*) views trained with 894 and 786 normal FFDMs from OPTIMAM Hologic dataset.

2.3 Mass Detection using High-Density Synthetic Data Augmentation

Our baseline model for mass detection in FFDM is a Deformable DETR [37] with a ResNet50 [38] feature extraction backbone. The model choice was based on the good performance of Deformable DETR in our previous comparative study [34]. The model was trained using mammograms with annotated masses from OPTIMAM Hologic from BI-RADS categories ranging from A to C, excluding BI-RADS D in the training phase. In this training setup, the model did not see any BI-RADS D images during training. The input size was 1332×800 pixel and only random flipping was used as data augmentation.

First, the baseline model was trained without synthetic data augmentation. Then, four other mass detection models were trained with synthetic data augmentation as follows. Three mass detection models, named *BC-Aug*, *CS-Aug* and *OP-Aug*, used synthetic images from a single CycleGAN model with a proportion of 1:1 per mammogram – 1 real and 1 synthetic. The fourth detection model included a combination of synthetic images from all the CycleGAN models described in Figure 3 with a proportion of 1:3 per mammogram – 1 real and 3 synthetic. The *BC-Aug* detection model

<https://github.com/junyanz/pytorch-CycleGAN-and-pix2pix>

was trained using synthetic data generated from the *BC-All* CycleGAN. The *OP-Aug* and the *CS-Aug* detection models were trained with synthetic data from the corresponding CycleGAN models. Note that *BC-All* generates both the MLO and CC views, whereas the CSAW and OPTIMAM have two independent models for each view: *CS-CC*, *CS-MLO*, *OP-CC* and *OP-MLO*. In the combined detection model the proportion of synthetic data was three times higher than the original data. All models were trained five times, that is, using five different random seeds, and evaluated by averaging the results across seeds. A single GPU was used (24GB NVIDIA GeForce RTX 3090) to train each model for a maximum of 60 epochs, using a batch size of 1 and adjusting the learning rate following the implementation recommendations of the MMDetection framework.

2.4 Reader Study

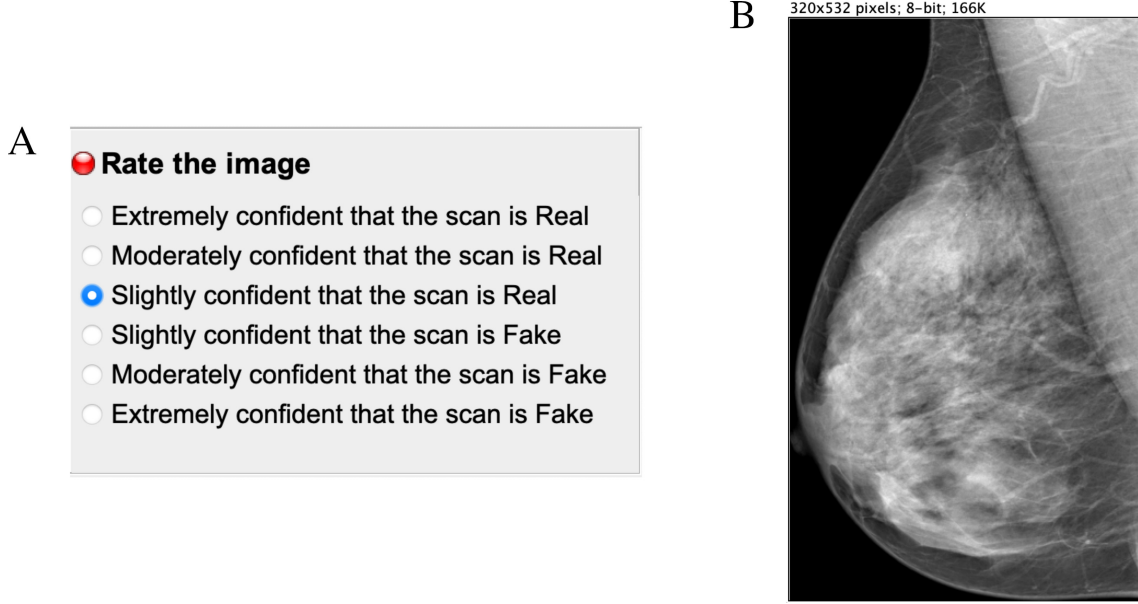


Figure 4: Main panels of the ImageJ reader study plugin. (A) multiple choice panel to label the mammograms as synthetic (Fake) or original (Real). (B) Mammogram image to assess.

A reader study involving 2 breast radiologists and 1 surgical oncologist specializing in breast disease was conducted to determine whether the synthetic images were distinguishable from the real ones as a proxy for perceptual realism. The participants were two breast radiologists from different hospitals in Spain, with +9 (Reader A) and +7 (Reader B) years of experience and the surgical oncologist from a hospital in Poland with +12 years of experience in image guided breast biopsy and lesion localization techniques (Reader C).

The reader study contained 180 high-density mammograms balanced by view and dataset. A total of 90 images were original BI-RADS D mammograms: 30 from OPTIMAM Hologic, 30 from CSAW and 30 from BCDR dataset. The other 90 images were synthetic mammograms generated with the different CycleGAN models: 30 images from *OP-CC* and *OP-MLO* models, 30 from *CS-CC* and *CS-MLO* models, and 30 from *BC-All* model. The original low-density mammograms used to generate the synthetic images were randomly selected from BI-RADS A OPTIMAM Hologic dataset.

The reader study was designed as a stand-alone ImageJ plugin. A single mammogram was displayed at a time (figure 4B) next to a multiple-choice panel (figure 4A) to assign a label based on the certainty of the image being synthetic (Fake) or original (Real). The 6 different choices were converted to equally-distributed probabilities of [0.95, 0.77, 0.59, 0.41, 0.23, 0.05] to compute the Receiver Operating Characteristic (ROC) curve of each reader as in [39]. No feedback was given to the readers during the assessment to avoid the identification of artifacts of synthetic images.

The images were resized to a maximum 532 pixels height to avoid the identification of the checkerboard artifacts and the lack of sharpness of synthetic mammograms, which is related to upsampling [40] in GANs. The goal of the reader test

<https://github.com/open-mmlab/mmdetection>
<https://imagej.nih.gov/ij/>

Table 2: Fréchet Inception Distance between different sets of images. The lower bound was defined as the FID between two different splits of real BI-RADS D mammograms from the same dataset. Similarly, the upper bound was given by the FID between real BI-RADS A and BI-RADS D mammograms. The input low-density images to all the CycleGAN models (*BC-All*, *CS-CC*, *CS-MLO*, *OP-CC* and *OP-MLO*) were real BI-RADS A mammograms from the OPTIMAM Hologic dataset.

	Dataset	View	# images	Real BI-RADS D (lower bound)	Synthetic BI-RADS D (CycleGAN model)	Real BI-RADS A (upper bound)
Real BI-RADS D	OPTIMAM	CC	148	34.17	73.16 (<i>OP-CC</i>)	107.99
	Hologic	MLO	179	57.24	109.68 (<i>OP-MLO</i>)	140.93
	CSAW	CC	101	42.57	99.95 (<i>CS-CC</i>)	142.34
		MLO	96	73.54	165.48 (<i>CS-MLO</i>)	206.04
	BCDR	CC + MLO	36	66.16	149.10 (<i>BC-All</i>)	142.61

was to evaluate the anatomically-plausible realism of the synthetic images rather than the noise and common artifacts of the CycleGAN models. Additionally, we asked radiologists to identify the artifacts and common pitfalls of the synthetic images after performing the reader study (Section 3.3.2).

3 Results

3.1 Evaluation for the CycleGAN models

The Fréchet Inception Distance (FID) [41] is a useful metric to measure the quality of the synthetic mammograms and compare the synthetic models with each other. The FID was calculated between two different sets of images. Since FID is not an absolute measure, we defined lower and upper bounds using real mammograms. First, the lower bound was defined as the FID between two different splits of real BI-RADS D mammograms from the same dataset. Second, the upper bound was given by the FID between real BI-RADS A and BI-RADS D mammograms. The synthetic BI-RADS D images in our evaluation set were generated using the five different CycleGAN models (*BC-All*, *CS-CC*, *CS-MLO*, *OP-CC* and *OP-MLO*). The input BI-RADS A mammograms to all the CycleGAN models were from the OPTIMAM dataset. In such manner, we would like to evaluate if the synthetic images are able to translate from the source domain – OPTIMAM Hologic – to the target domains – OPTIMAM Hologic, CSAW or BCDR – with enough fidelity.

In Table 2, the FID between different groups of images is shown. Ideally, the FID between synthetic and real BI-RADS D mammograms should be as close as possible to the lower bound and do not exceed the upper bound. As an example, the FID in CSAW CC view between real and synthetic BI-RADS D (generated using *CS-CC* model) was 99.95, which is between the lower bound (42.57) and the upper bound (142.34). Moreover, the FID in CSAW is lower in CC view (99.95) than in the MLO view (165.48). Both in OPTIMAM Hologic and CSAW datasets, the FID between the real and the synthetic BI-RADS D mammograms lies between the FID bounds. Moreover, the FID score was lower for the synthetic CC mammograms than for the MLO view. Only in BCDR, the FID score was greater than the FID between both original images.

3.1.1 Qualitative Analysis of the synthetic images

In Figure 5 there are some sample high-density mammograms generated with the different CycleGAN models. The first row (Figure 5:A) corresponds to the CC view and the second (Figure 5:B) to MLO. The first column is the original BI-RADS A FFDMs from OPTIMAM Hologic scanner. The next columns are the synthetic FFDMs from the different CycleGAN models. By visual inspection, one can see that the synthetic images did not remove the masses in the original mammograms, which enabled their usage for data augmentation in the mass detection training. We can also confirm that the synthetic images are able to properly translate from source to target domain. The low-to-high-density image translation was applied for the input BI-RADS A, B, or C. In higher density mammograms, such as BI-RADS C, the changes were more subtle and less density was added to the output image.

3.2 Mass Detection Performance

The area under the curve (AUC) of the Free-response Receiver Operating Characteristic (FROC) curve [42] was used to compare the baseline with the different data augmentation strategies in the test sets. The AUC was computed by varying the confidence threshold of each bounding box in a range of $FPPI \in [0, 1]$. If the Intersection-over-Union (IoU) of the prediction and the ground truth was greater than 10%, then the bounding box was a true positive (TP).

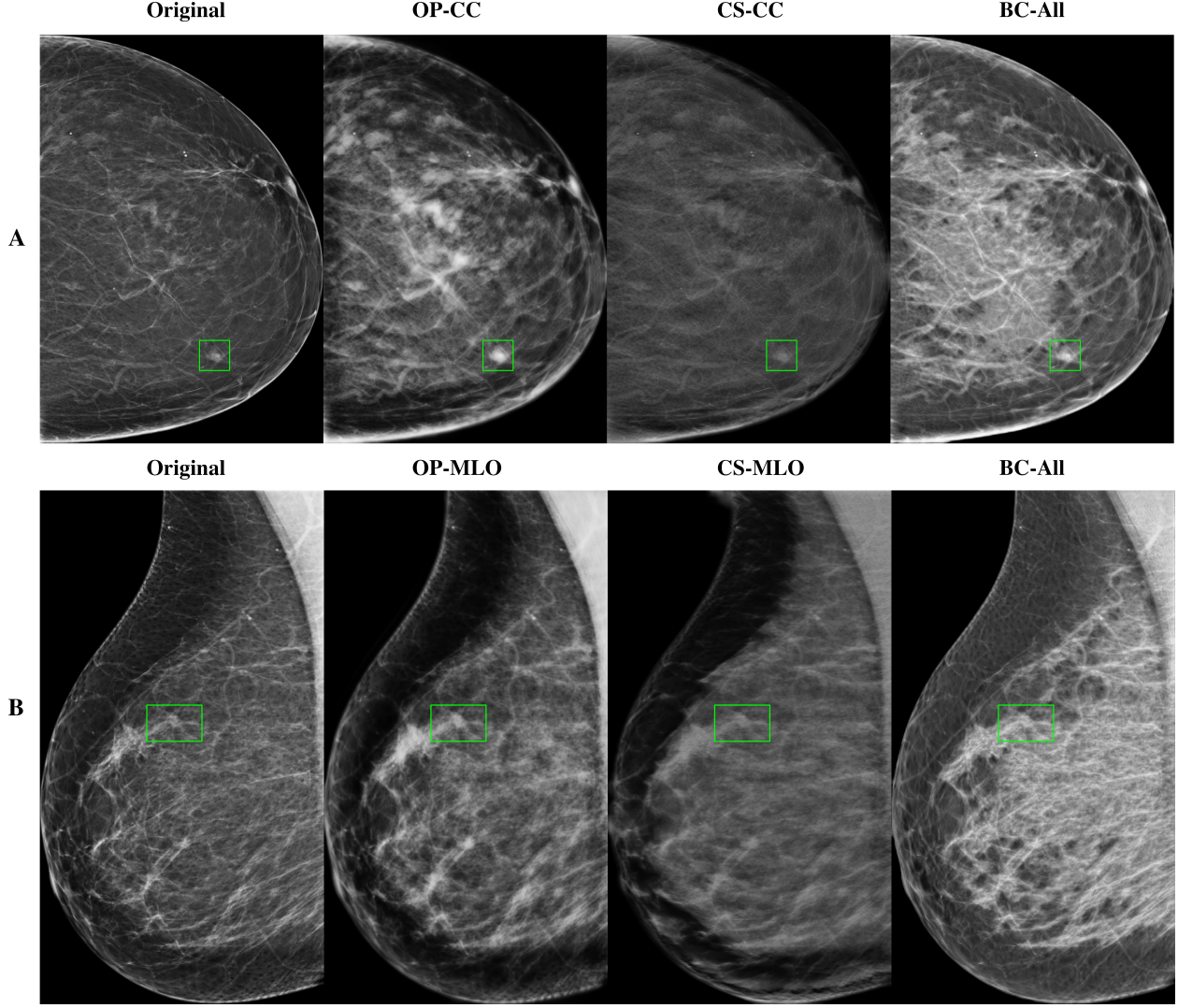


Figure 5: Samples of high-density synthetic mammograms generated with the different CycleGAN models. On the left, the input BI-RADS A mammogram from OPTIMAM Hologic dataset. (A) CC view, (B) MLO view.

The first test set contained BI-RADS D mammograms from OPTIMAM Hologic, a total of 161 (see Table 1 MMG with masses). The corresponding FROC curves are shown in Figure 6:A. The AUC for the combined data augmentation strategy had the best improvement in comparison to the baseline – a 2% gain in AUC, from 0.82 to 0.84. The data augmentation strategies using a single CycleGAN model for data synthesis did not improve the AUC. Only a 1% gain in AUC was obtained with the *OP-Aug* detection model, from 0.82 to 0.83.

The mammograms with masses from the INbreast dataset were used as an external dataset to evaluate the training strategies (Figure 6:B). The *BC-Aug* detection model had the highest gain in AUC – a total of 6% gain, improving from 0.83 to 0.89. Both INbreast and BCDR datasets contain FFDs from Siemens scanners. The combined strategy had a 3% AUC improvement in comparison to the baseline, from 0.83 to 0.86. Figure 7 shows that not only the Sensitivity but also the Precision was improved when using high-density synthetic data in training.

3.3 Reader Study Outcomes

3.3.1 Receiver Operating Characteristic Curves

The area under the curve (AUC) of each reader Receiver Operating Characteristic (ROC) can be found in Table 3. On average, the synthetic mammograms of CC view from OPTIMAM CycleGAN were the most difficult to discriminate

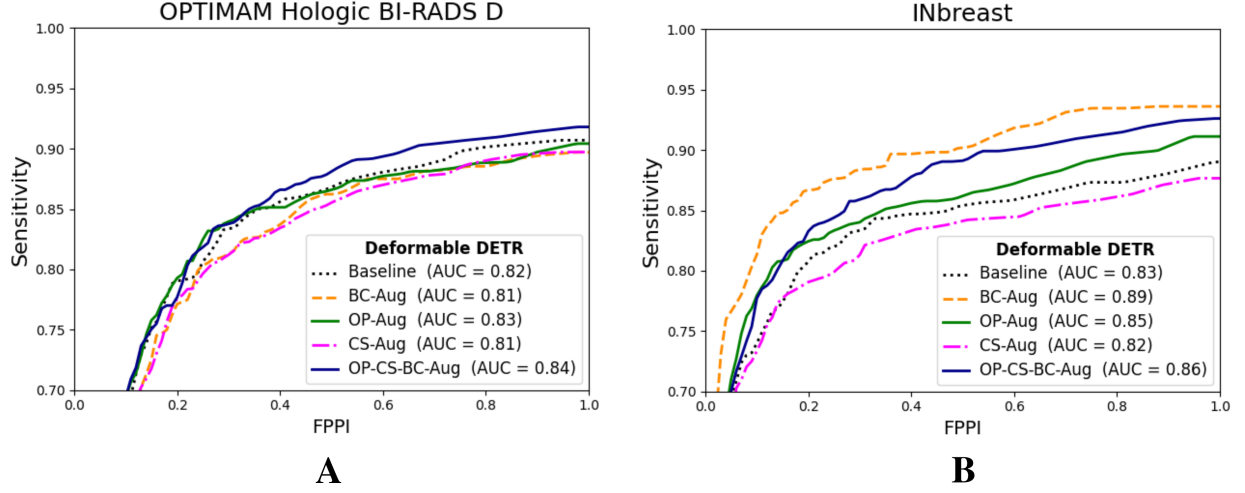


Figure 6: Free-response Receiver Operating Characteristic (FROC) curves for the different mass detection models, averaged over a total of 5 random seeds per model. The baseline model did not include synthetic data augmentation in the training. The *BC-Aug*, *CS-Aug* and *OP-Aug* models only used synthetic images from the corresponding CycleGAN models with a proportion of 1:1 per mammogram – 1 real and 1 synthetic. The combined model used synthetic images from the three different models with a proportion of 1:3 per mammogram – 1 real and 3 synthetic. **(A)** OPTIMAM Hologic test set containing 161 BI-RADS D mammograms with annotated masses, **(B)** INbreast test set containing 108 mammograms with annotated masses from different breast densities.

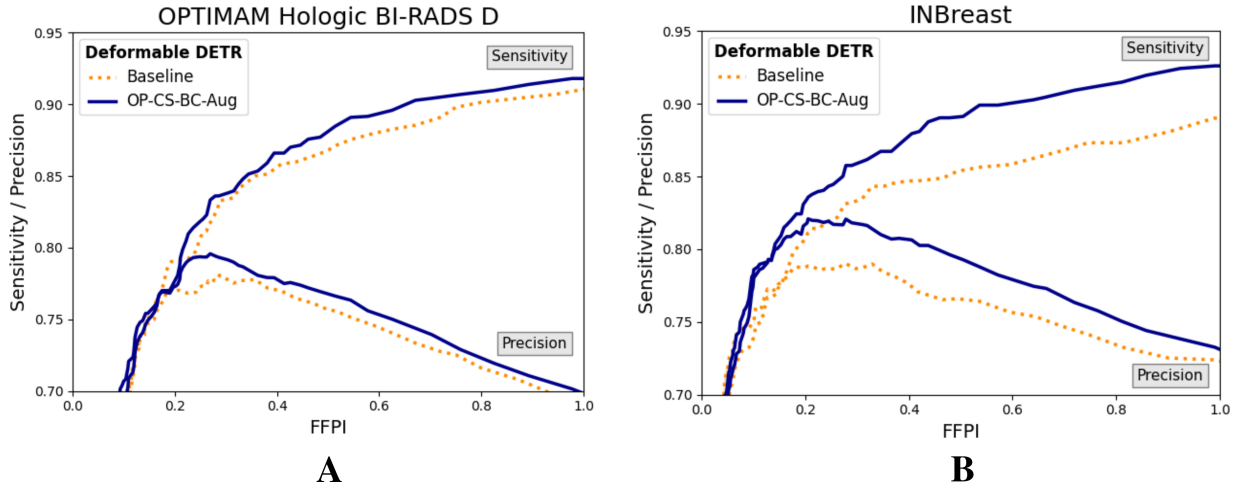


Figure 7: Sensitivity versus Precision plots. The baseline model did not include synthetic data augmentation in the training. The combined model used synthetic images from the three different models with a proportion of 1:3 per mammogram – 1 real and 3 synthetic. **(A)** OPTIMAM Hologic test set containing 161 BI-RADS D mammograms with annotated masses, **(B)** INbreast test set containing 108 mammograms with annotated masses from different breast densities.

from original mammograms (0.615 AUC). Overall, the CC view looked more realistic to all participants than the MLO view. The BCDR model was the easiest for recognition of synthetic images, with an AUC of 0.824 in CC view and 0.954 in MLO view.

3.3.2 Qualitative Analysis of Synthetic FFDM

After completing the reader study, the participants evaluated the realism of the synthetic images and identified the common artifacts and failures.

Table 3: Reader test results: Area Under the Curve (AUC) from the Receiver Operating Characteristics (ROC) curve of each CycleGAN model and view (CC, MLO). Reader A: 9+ years of experience as a breast radiologist. Reader B: 7+ years of experience as a breast radiologist. Reader C: surgical oncologist with +12 years of experience in image guided breast biopsy and lesion localization techniques.

	OPTIMAM		CSAW		BCDR	
	CC	MLO	CC	MLO	CC	MLO
Reader A	0.580	0.664	0.651	0.718	0.818	0.962
Reader B	0.576	0.893	0.887	0.758	0.871	0.956
Reader C	0.689	0.673	0.489	0.636	0.784	0.944
Average	0.615	0.743	0.675	0.704	0.824	0.954

Common Artifacts and Failures The most unrealistic features in order of importance were: 1) big concentrations of glandular tissue adjacent to pectoral muscle (Figure 8:D); 2) dark small dots or ovals in the image like perforations (figure 8:A); 3) linear fragmentation of muscles; 4) distorted nipples (Figure 8:C); and 5) lack of glandular tissue behind the nipple (figure 8:B). Some synthetic images missed to preserve the prepectoral fat or smooth contours at the interface with subcutaneous fat.

Realistic Mammograms Some synthetic high-density FFDMs that looked realistic to the radiologist are shown in Figure 9. The features that improved realism of synthetic images were 1) the presence of linear microcalcifications or roundish calcifications; 2) lymph nodes in the correct areas; 3) post-biopsy tissue markers; and 4) the correct distribution of dense tissue.

4 Discussion

The contributions in this study are two fold. First, synthesize high-resolution high-density FFDMs from different domains. Second, use the synthetic images as data augmentation to improve the mass detection performance in high-density breasts and multi-center datasets.

In our image synthesis experiments, we trained a total of five CycleGAN models using FFDMs from three different datasets to perform low-to-high density translation from real mammograms. Only healthy mammograms were used to train the image-to-image translation models. By training with healthy images, the models learned the healthy data distribution, hence, minimizing any risk of inserting hallucinated lesions into the synthetic images. As our goal was to use the synthetic mammograms to improve the mass detection, we confirmed that the CycleGAN models did not remove the masses from the original mammograms (see Figure 5).

To assess the quality of the synthetic images we calculated the commonly used FID metric between synthetic and real high-density mammograms. Since FID is not an absolute measure, we defined lower and upper bounds using real mammograms. The closer the synthetic images are to the real BI-RADS D images, the closer the FID should be to the lower bound. After evaluating the FID metric of the different CycleGAN models, we observed that the FID for the CC view was better than the one of the MLO view. The difficulty of synthesising MLO view was previously mentioned in [24], most probably because MLO has greater complexity and more anatomical information than the CC view. However, the *OP-MLO* and *CS-MLO* models still had an FID score between the lower and upper bounds. The worst performing model, based on the FID metric, was the *BC-All* CycleGAN. The synthetic images from the *BC-All* model had an FID score greater than the upper threshold. There are two major reasons why the FID score of *BC-All* synthetic images was closer to real low density images than to high-density ones. First, the *BC-All* model combined both views in the training and was the model with less training data (see Figure 3:A). Second, and more important, there was a big domain difference between the source domain, BI-RADS A mammograms from OPTIMAM Hologic, and the target domain, BI-RADS D mammograms from BCDR dataset. BCDR contains old digitised film mammograms acquired using a Siemens scanner while OPTIMAM is a Hologic digital mammography dataset with very specific image characteristics, i.e., it is very sharp, usually shows lymph nodes very well and it does visualize some skin of the breast.

To further evaluate the clinical realism of the synthetic images, we performed a reader study involving 2 breast radiologists and 1 surgical oncologist. When the CycleGAN models trained using OPTIMAM Hologic and CSAW datasets (*OP-CC*, *OP-MLO*, *CS-CC*, *CS-MLO*) were used to insert density onto low density mammograms from OPTIMAM Hologic, it was much more difficult for the readers to differentiate between original and synthetic mammograms. In that case, the readers had to look for anatomical disparities and inadequacies to spot the difference. Both OPTIMAM and CSAW FFDMs were acquired with an Hologic scanner. On the other hand, all the readers could easily identify the synthetic images generated with the *BC-All* model. As previously mentioned, BCDR contains old digitised film

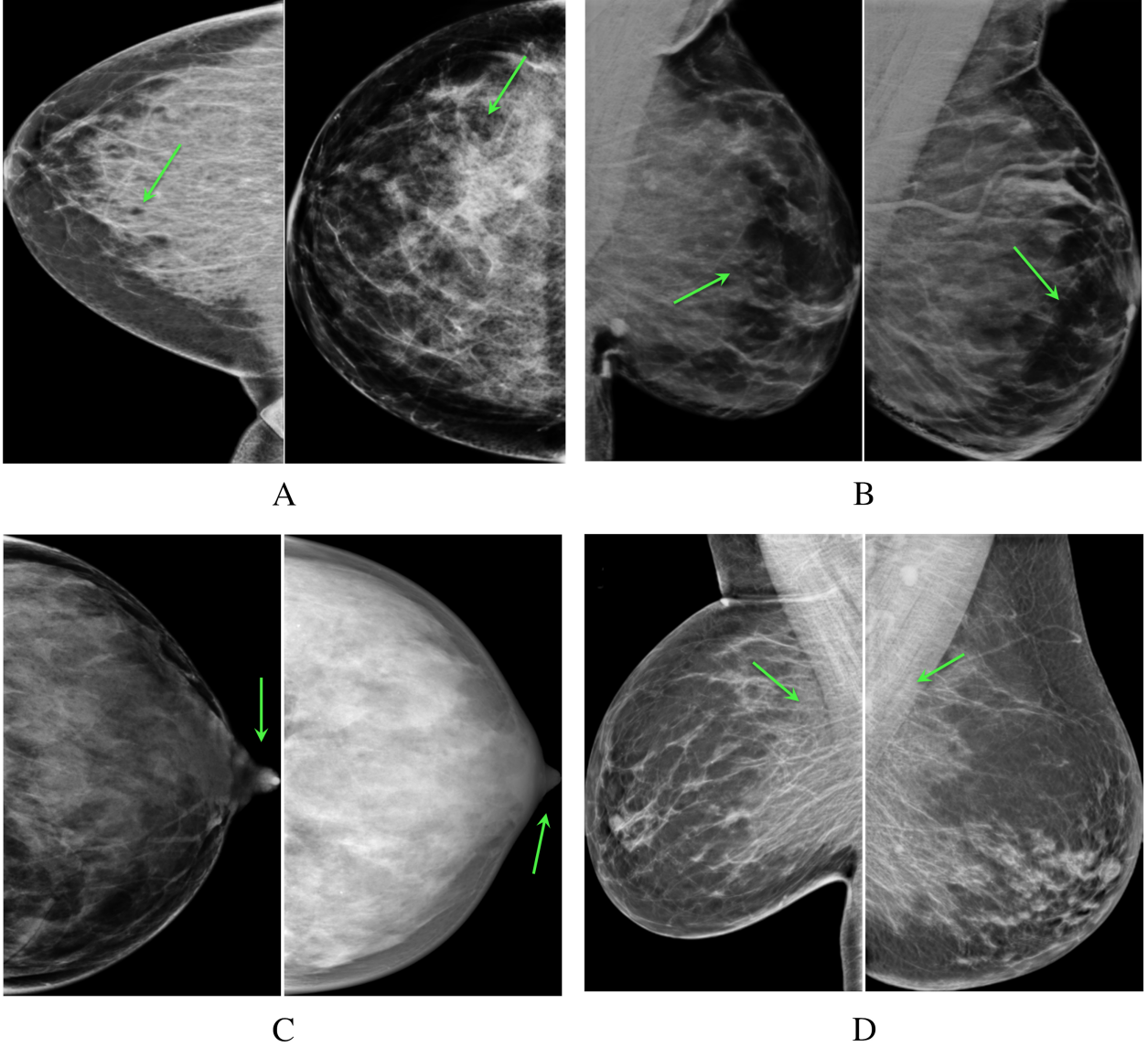


Figure 8: Common artifacts of synthetic high-density mammograms, (A) dark dots or ovals, (B) lack of glandular tissue behind the nipple, (C) distorted nipples, (D) big concentrations of glandular tissue adjacent to the pectoral muscle.

mammograms acquired with a Siemens scanner. Considering that, we can conclude that domain disparities between the acquisition settings of the source and the target domains have a big impact in the perceptual realism of the synthetic images. In addition, the synthetic mammograms from the MLO view were easier to identify than the ones from the CC view. Overall, we confirmed that the outcomes from the reader study correlate with the FID scores of the CycleGAN models.

In our mass detection experiments, different data augmentation strategies were tested to improve the mass detection of the baseline model. First, three mass detection models were trained using synthetic images from the different CycleGANs with a proportion of 1:1 – 1 real and 1 synthetic. Second, a fourth mass detection model was trained with synthetic images from all the CycleGAN models with a proportion of 1:3 – 1 real and 3 synthetic. This last mass detection model, named **OP-CS-BC-Aug**, achieved the best performance in OPTIMAM BI-RADS D test set (see Figure 6:A), showing the potential of our synthetic data augmentation to improve detection in high-density breasts.

The same strategy also improved the mass detection performance in the INbreast test set (Figure 6:B). INbreast is an external validation dataset that comprises mammograms from another domain and includes different breasts densities. However, the best data augmentation strategy in INbreast, the *BC-Aug* model, used only synthetic data from the

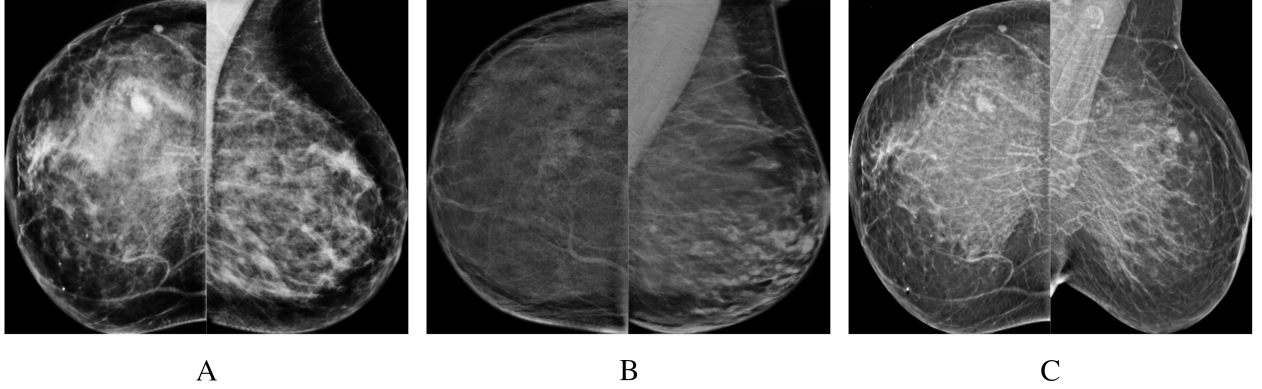


Figure 9: Synthetic high-density mammograms that looked realistic to the radiologist. Samples from the different CycleGAN models: (A) *OP-CC* and *OP-MLO*, (B) *CS-CC* and *CS-MLO*, (C) *BC-All*.

BC-All CycleGAN model. The *BC-Aug* detection model achieved an AUC of 0.89 while the combined strategy (the *OP-CS-BC-Aug* model) only reached an AUC of 0.86. Even though both data augmentation strategies improved the baseline performance in INbreast (0.83 AUC), using the synthetic data from the *BC-All* model helped the final model to generalize better. One reason for that can be that the *BC-All* model was trained with images from the BCDR dataset, which were acquired with the same scanner manufacturer (Siemens) than INbreast mammograms.

As we hypothesized, the CycleGAN models not only learned how to translate from low-to-high density but also acted as a domain adaptation technique translating the domain characteristics from dataset used to train the generative models. The domain characteristics include the differences in image quality, acquisition settings and scanner manufacturers.

Fairer comparisons could be achieved if we had more images in the datasets for each generative model. This is the most common and general limitation in the medical imaging AI research due to the scarcity of expert annotated images. In tasks where patch-based approaches are sufficient, extracting multiple samples from one scan can aid to overcome the data scarcity issue. However, this limitation is further exacerbated in tasks where a single subject scan can only be used as a single sample in the training of deep learning methods. Moreover, the high resolution nature of the breast FFDMs makes it even more challenging. We believe that this study is not only an important step towards mitigating data scarcity and class imbalance, but also demonstrates the importance of fair AI in clinical practice. However, there is still room for improvement to increased the fairness of AI models for women with high-density breasts in mammography screening. Future research may focus on evaluating the potential of the high-density synthetic mammograms in other downstream tasks, such as classification or segmentation, by means of data augmentation. Also, improving the generative models using the feedback provided by the reader study.

5 Conclusion

In this study, we evaluated different CycleGAN models for high-density FFDM synthesis from three different datasets and acquisition pipelines, comprising two scanner manufacturers – i.e. Hologic and Siemens. Moreover, we tried different synthetic data augmentation strategies to improve the mass detection performance of a deep-learning based model. The results demonstrated that the data augmentation helped to improve the mass detection in two test sets, one comprising *BI-RADS D* mammograms from the same domain used for training and another not seen in the training, improving the domain generalization of the final model. Finally, a reader study involving three expert radiologists evaluated the perceptual realism of the synthetic mammograms, concluding that the quality of CC view synthetic images is higher than the mammograms from MLO view. Our study is the first one to synthesize high-resolution FFDMs with increased density and showed the potential of including the generated images in the data augmentation pipeline to improve the generalization and performance of downstream tasks using mammography images (from different sources), such as mass detection.

Conflict of Interest Statement

The authors declare that the research was conducted in the absence of any commercial or financial relationships that could be construed as a potential conflict of interest.

Author Contributions

LG, KK, RO and OD contributed to the conception and design of the study. LG organized the datasets, performed the experiments and designed the reader study. BC, AC and JR participated in the reader study and clinical assessment of the results. FD contributed with one dataset (CSAW) in this study. LI and KL supervised the research. All authors contributed to article revision and read and approved the submitted version.

Funding

This project has received funding from the European Union’s Horizon 2020 research and innovation programme under grant agreement No 952103. This work was supported in part by the MICINN Grant RTI2018-095232-B-C21 and 2017 SGR 1742.

Acknowledgments

A subset of the OPTIMAM database was obtained as part of the data-sharing agreement with the University of Barcelona in 2021. Special thanks to Volpara Health (Dr Melissa Hill) for agreeing to share the breast density information of the OPTIMAM subset used and to Dr Premkumar Elanvogan to share the base code to prepare the ImageJ plugin for the reader study.

Data Availability Statement

The CycleGAN models generated for this study can be found in the *medigan* [43] GitHub repository .

Ethics Statement

Written informed consent for participation was not required for this study in accordance with the national legislation and the institutional requirements.

References

- [1] C.J. D’Orsi, E.A. Sickles, E.B. Mendelson, and E.A. Morris. *ACR BI-RADS® Atlas, Breast Imaging Reporting and Data System (ACR BI-RADS® Magnetic Resonance Imaging)*. American College of Radiology, Reston, VA, 2013.
- [2] K. Pesce, M. Tajerian, M.J. Chico, M.P. Swiecicki, B. Boietti, M.J. Frangella, and et. al. Interobserver and intraobserver variability in determining breast density according to the fifth edition of the BI-RADS® Atlas. *Radiologia (English Edition)*, 62(6):481–486, 2020.
- [3] Brian L. Sprague, Ronald E. Gangnon, Veronica Burt, Amy Trentham-Dietz, John M. Hampton, Robert D. Wellman, and et. al. Prevalence of Mammographically Dense Breasts in the United States. *JNCI: Journal of the National Cancer Institute*, 106(10), 2014.
- [4] Yunan Han, Justin Xavier Moore, Graham A. Colditz, and Adetunji T. Toriola. Family History of Breast Cancer and Mammographic Breast Density in Premenopausal Women. *JAMA Network Open*, 5(2):e2148983–e2148983, 2022.
- [5] Karla Kerlikowske, Weiwei Zhu, Anna NA Tosteson, Brian L Sprague, Jeffrey A Tice, Constance D Lehman, Diana L Miglioretti, and Breast Cancer Surveillance Consortium*. Identifying women with dense breasts at high risk for interval cancer: a cohort study. *Annals of internal medicine*, 162(10):673–681, 2015.
- [6] Norman F. Boyd, Helen Guo, Lisa J. Martin, Limei Sun, Jennifer Stone, Eve Fishell, Roberta A. Jong, and et. al. Mammographic density and the risk and detection of breast cancer. *New England Journal of Medicine*, 356(3):227–236, 2007.
- [7] Fredrik Strand, Edward Azavedo, Roxanna Hellgren, Keith Humphreys, Mikael Eriksson, John Shepherd, Per Hall, and et. al. Localized mammographic density is associated with interval cancer and large breast cancer: a nested case-control study. *Breast Cancer Research*, 21(1):1–9, 2019.

<https://github.com/RichardObi/medigan>

- [8] Jean Morag Seely, Susan Elizabeth Peddle, Huiming Yang, Anna M. Chiarelli, Megan McCallum, Gopinath Narasimhan, and et. al. Breast density and risk of interval cancers: The effect of annual versus biennial screening mammography policies in canada. *Canadian Association of Radiologists Journal*, 73(1):90–100, 2022.
- [9] Paula B. Gordon. The impact of dense breasts on the stage of breast cancer at diagnosis: A review and options for supplemental screening. *Current Oncology*, 29(5):3595–3636, 2022.
- [10] Valerie A McCormack and Isabel dos Santos Silva. Breast density and parenchymal patterns as markers of breast cancer risk: a meta-analysis. *Cancer Epidemiology Biomarkers & Prevention*, 15(6):1159–1169, 2006.
- [11] Sherry Yueh-Hsia Chiu, Stephen Duffy, Amy Ming-Fang Yen, Laszlo Tabár, Robert A. Smith, and Hsiu-Hsi Chen. Effect of Baseline Breast Density on Breast Cancer Incidence, Stage, Mortality, and Screening Parameters: 25-Year Follow-up of a Swedish Mammographic Screening. *Cancer Epidemiology, Biomarkers and Prevention*, 19(5):1219–1228, 2010.
- [12] Natalie J. Engmann, Marzieh K. Golmakani, Diana L. Miglioretti, Brian L. Sprague, Karla Kerlikowske, and et. al. Population-Attributable Risk Proportion of Clinical Risk Factors for Breast Cancer. *JAMA Oncology*, 3(9):1228–1236, 2017.
- [13] Daniëlle van der Waal, Theodora M. Ripping, André L.M. Verbeek, and Mireille J.M. Broeders. Breast cancer screening effect across breast density strata: A case–control study. *International Journal of Cancer*, 140(1):41–49, 2017.
- [14] Stefanie Weigel, W. Heindel, J. Heidrich, H.-W. Hense, and O. Heidinger. Digital mammography screening: sensitivity of the programme dependent on breast density. *European Radiology*, 27(7):2744–2751, 2017.
- [15] Ian Goodfellow, Jean Pouget-Abadie, Mehdi Mirza, Bing Xu, David Warde-Farley, Sherjil Ozair, and et al. Generative Adversarial Nets. In Z. Ghahramani et al, editor, *Advances in Neural Information Processing Systems*, volume 27, pages 2672–2680. Curran Associates, Inc., 2014.
- [16] Parita Oza, Paawan Sharma, Samir Patel, Festus Adedoyin, and Alessandro Bruno. Image augmentation techniques for mammogram analysis. *Journal of Imaging*, 8(5):141, 2022.
- [17] Richard Osuala, Kaisar Kushibar, Lidia Garrucho, Akis Linardos, Zuzanna Szafranowska, Stefan Klein, and et al. A review of generative adversarial networks in cancer imaging: new applications, new solutions [Online]. *arXiv [Preprint]*, 2021.
- [18] Manal AlAmir and Manal AlGhamdi. The Role of Generative Adversarial Network in Medical Image Analysis: An in-Depth Survey. *ACM Comput. Surv.*, mar 2022. Just Accepted.
- [19] Anton S. Becker, Lukas Jendele, Ondrej Skopek, Nicole Berger, Soleen Ghafoor, Magda Marcon, and et. al. Injecting and removing suspicious features in breast imaging with CycleGAN: A pilot study of automated adversarial attacks using neural networks on small images. *European Journal of Radiology*, 120:108649, 2019.
- [20] Cyril Zakka, Ghida Saheb, Elie Najem, and Ghina Berjawi. Mammoganesis: Controlled generation of high-resolution mammograms for radiology education [internet]. *arXiv [Preprint]*, 2020.
- [21] Shrinivas D Desai, Shantala Giraddi, Nitin Verma, Puneet Gupta, and Sharan Ramya. Breast cancer detection using gan for limited labeled dataset. In *2020 12th International Conference on Computational Intelligence and Communication Networks (CICN)*, pages 34–39, 2020.
- [22] Lukas Jendele, Ondrej Skopek, Anton S Becker, and Ender Konukoglu. Adversarial augmentation for enhancing classification of mammography images [Internet]. *arXiv [Preprint]*, 2019.
- [23] Chisako Muramatsu, Mizuho Nishio, Takuma Goto, Mikinao Oiwa, Takako Morita, Masahiro Yakami, and et. al. Improving breast mass classification by shared data with domain transformation using a generative adversarial network. *Computers in Biology and Medicine*, 119:103698, 2020.
- [24] Dimitrios Korkinof, Tobias Rijken, Michael O’Neill, Joseph Yearsley, Hugh Harvey, and Ben Glocker. High-resolution mammogram synthesis using progressive generative adversarial networks [internet]. *arXiv [Preprint]*, 2018.
- [25] Tero Karras, Timo Aila, Samuli Laine, and Jaakko Lehtinen. Progressive growing of gans for improved quality, stability, and variation. In *6th International Conference on Learning Representations*, Vancouver, BC, Canada, 2018. Conference Track Proceedings.
- [26] Dimitrios Korkinof, Hugh Harvey, Andreas Heindl, Edith Karpati, Gareth Williams, Tobias Rijken, Peter Kecskemethy, and Ben Glocker. Perceived realism of high-resolution generative adversarial network–derived synthetic mammograms. *Radiology. Artificial intelligence*, 3(2), 2021.

- [27] Kenny H. Cha, Nicholas A. Petrick, Aria X. Pezeshk, Christian G. Graff, Diksha Sharma, Andreu Badal, and et. al. Evaluation of data augmentation via synthetic images for improved breast mass detection on mammograms using deep learning. *Journal of Medical Imaging*, 7(1):1–9, 2019.
- [28] Aldo Badano, Christian G. Graff, Andreu Badal, Diksha Sharma, Rongping Zeng, Frank W. Samuelson, and et al. Evaluation of Digital Breast Tomosynthesis as Replacement of Full-Field Digital Mammography Using an In Silico Imaging Trial. *JAMA Network Open*, 1(7):e185474–e185474, 11 2018.
- [29] Mark D Halling-Brown, Lucy M Warren, Dominic Ward, Emma Lewis, Alistair Mackenzie, and Matthew G Wallis. OPTIMAM mammography image database: A large-scale resource of mammography images and clinical data. *Radiology: Artificial Intelligence*, 3(1):e200103, 2021.
- [30] Karin Dembrower, Peter Lindholm, and Fredrik Strand. A multi-million mammography image dataset and population-based screening cohort for the training and evaluation of deep neural networks—the cohort of screen-aged women (CSAW). *Journal of digital imaging*, 33(2):408–413, 2020.
- [31] Brad M Keller, Jinbo Chen, Dania Daye, Emily F Conant, and Despina Kontos. Preliminary evaluation of the publicly available Laboratory for Breast Radiodensity Assessment (LIBRA) software tool: comparison of fully automated area and volumetric density measures in a case–control study with digital mammography. *Breast Cancer Research*, 17(1):1–17, 2015.
- [32] Miguel G Lopez, Naimy Posada, Daniel C Moura, Raúl Ramos Pollán, José M Franco Valiente, César Suárez Ortega, and et. al. Bcdr: a breast cancer digital repository, 2012.
- [33] Inês C. Moreira, Igor Amaral, Inês Domingues, António Cardoso, Maria João Cardoso, and Jaime S. Cardoso. INbreast: toward a full-field digital mammographic database. *Academic radiology*, 19(2):236–248, 2012.
- [34] Lidia Garrucho, Kaisar Kushibar, Socayna Jouide, Oliver Diaz, Laura Igual, and Karim Lekadir. Domain generalization in deep learning based mass detection in mammography: A large-scale multi-center study. *Artificial Intelligence in Medicine*, 132:102386, 2022.
- [35] J. Zhu, T. Park, P. Isola, and A. A. Efros. Unpaired image-to-image translation using cycle-consistent adversarial networks. In *2017 IEEE International Conference on Computer Vision (ICCV)*, pages 2242–2251, Los Alamitos, CA, USA, 2017. IEEE Computer Society.
- [36] Joseph Paul Cohen, Margaux Luck, Sina Honari, and et al. Distribution matching losses can hallucinate features in medical image translation. In *International conference on medical image computing and computer-assisted intervention*, pages 529–536, Cham, 2018. Springer International Publishing.
- [37] Xizhou Zhu, Weijie Su, Lewei Lu, Bin Li, Xiaogang Wang, and Jifeng Dai. Deformable DETR: Deformable Transformers for End-to-End Object Detection. In *International Conference on Learning Representations*, 2021.
- [38] Kaiming He, Xiangyu Zhang, Shaoqing Ren, and Jian Sun. Deep residual learning for image recognition. In *Proceedings of the IEEE conference on computer vision and pattern recognition*, pages 770–778, 2016.
- [39] Basel Alyafi, Oliver Diaz, Premkumar Elangovan, Joan C. Vilanova, Javier del Riego, and Robert Martí. Quality analysis of DCGAN-generated mammography lesions. In Hilde Bosmans, Nicholas Marshall, and Chantal Van Ongeval, editors, *15th International Workshop on Breast Imaging (IWBI2020)*, volume 11513, pages 80–85. SPIE, 2020.
- [40] Augustus Odena, Vincent Dumoulin, and Chris Olah. Deconvolution and checkerboard artifacts. *Distill [Internet]*, 2016.
- [41] Martin Heusel, Hubert Ramsauer, Thomas Unterthiner, Bernhard Nessler, and Sepp Hochreiter. GANs Trained by a Two Time-Scale Update Rule Converge to a Local Nash Equilibrium. In I. Guyon and et. al., editors, *Advances in Neural Information Processing Systems*, volume 30, page 6629–6640. Curran Associates, Inc., 2017.
- [42] Andriy I Bandos, Howard E Rockette, Tao Song, and David Gur. Area under the free-response ROC curve (FROC) and a related summary index. *Biometrics*, 65(1):247–256, 2009.
- [43] Richard Osuala, Noussair Lazrak, Kaisar Kushibar, Lidia Garrucho, Socayna Jouide, Grzegorz Skorupko, and et al. mediGAN: Synthetic Medical Data From Pretrained Generative Models (version 0.1), mar 2022.